A Simple Transfer Learning Approach for Assessing Small Datasets in Electrochemical Energy Cells Manufacturing

Francisco Fernandez[1,2], Soorya Saravanan[1,2], Rashen Lou Omongos [1,2], Javier F. Troncoso[1,2], Diego E. Galvez-Aranda[1,2], Alejandro A. Franco[1,2,3,4*]

[1] Laboratoire de Réactivité et Chimie des Solides (LRCS), Université de Picardie Jules Verne, Hub de l'Energie, UMR CNRS 7314,15 rue Baudelocque, 80039 Amiens, France

[2] Réseau sur le Stockage Electrochimique de l´Energie (RS2E), FR CNRS 3459, Hub de l'Energie, 15 rue Baudelocque, Amiens Cedex, 80039, France

[3] ALISTORE-European Research Institute, FR CNRS 3104, Hub de l'Energie, 15 rue Baudelocque, Amiens Cedex, 80039 France

[4] Institut Universitaire de France, 103 Boulevard Saint Michel, Paris, 75005, France

∗Corresponding author: alejandro.franco@u-picardie.fr

Abstract

The performance of electrochemical cells for energy storage and conversion, such as batteries and fuel cells, can be improved by optimizing their manufacturing processes. This can be very time consuming and costly through the conventional trial-and-error approaches. Machine Learning (ML) models can help to accelerate finding solutions to these types of problems. In academic research laboratories, manufacturing dataset sizes can be small, while ML models typically require large amounts of data. In this work, we propose a simple Transfer Learning (TL) approach where a Neural Network (NN) is trained in a vast dataset. Then, this NN is transferred to smaller datasets by freezing its weights and adding an extra trainable layer to improve the performance of this new TL-based NN. This novel approach is tested with pre-existing manufacturing experimental and stochastically generated datasets that were not acquired with the purpose of training ML models.

Introduction

Electrochemical energy cells (EECs) are devices that work through a redox (reduction-oxidation) reaction. Between them we have energy storage devices, like Lithium-Ion Batteries (LIBs) cells, and energy conversion devices, like Proton Exchange Membrane Fuel Cells (PEMFCs). Both applications play a crucial role towards the green transition needed to mitigate climate change. Given the intermittent production of renewable energy sources and an on-demand consumption requirement, EECs can help to better integrate these energy sources into the energy matrix. On one side, LIBs present a high energy density, extended lifespan, and low self-discharge that has significantly impacted various industries, including electronics and telecommunications, and served as key components in portable devices.[1] [2] LIBs are also contributing to the electrification of the transportation industry by being used in electric vehicles (EVs). [3] On the other side, PEMFCs presents high efficiency, low operating temperature and zero carbon emissions[4] and can act as an alternative application where EVs face limitations, such as heavy-duty trucks. However, despite the mentioned advantages, both LIBs and PEMFCs face challenges requiring further research and development efforts to optimize their manufacturing processes to attain better performance and efficiency.[5,6]

The redox reaction in a commercial LIB cell occurs at its main components, the positive and the negative electrode, and the final electrochemical performance of an electrode depends on their microstructure, which is highly influenced by the manufacturing process.[7] The manufacturing process includes different stages, the first of them is the slurry preparation, which consists of mixing active material (AM), electron conductive additive, binder, and solvent. This is followed by the slurry coating over the current collector. Then, since this is a wet process, it is followed by the drying step, where the solvent is evaporated to get the dried electrode. Then, the electrode is calendered to improve the contact between the electrode and the current collector and to reduce the overall thickness, which improves the cell energy density. By controlling these manufacturing parameters, like the AM chemistry selected for the slurry preparation or the gap and the speed in the rolls during calendering, we are able to also control the electrode microstructure. Therefore, the effect of these manufacturing parameters on the final electrode properties (density, porosity, mass loading, tortuosity factor) must be well understood to choose the best set of parameters that allow the optimization of the LIB cell performance.[8–10]

For PEMFCs, the Gas Diffusion Layer (GDL) is one of the most important components controlling the electrical and thermal conduction, reactant gases' dispersion and diffusion, and water management, which ultimately affects the PEMFC's performance. The three main stages of the GDL manufacturing involve carbon fiber production, followed by carbon paper substrate preparation and lastly, the finishing treatment. Starting with a wet-spinning step, polyacrylonitrile (PAN)-derived carbon fibers are processed into precursor fibers. These carbon fibers are sized and chopped after stabilization and carbonization. To improve the mechanical stability, conductivity, and reach desired porosity, a step involving the previous carbon fibers, mixed with water and binder, are then subjected to papermaking, bonding, impregnation, curing, and carbonization steps. Finally, the GDL substrate is dipped in polytetrafluoroethylene (PTFE). By varying the manufacturing parameters involved in the mentioned steps, such as the weight percentage of carbon and PTFE loading, this can ultimately affect the properties of the GDL such as electronic and thermal conductivities, porosity and tortuosity.[11,12] Which makes also this manufacturing process relevant for the optimization of the GDL performance.

For many years, numerous studies based on experimental approaches have been conducted to gain insight into the electrochemical, physical and mechanical phenomena in LIB electrodes and PEMFC GDLs.[13–23] The goal is to help understand the relationship between input factors and responses.[23] However, designing experiments is a complex process due to the large number of input parameters and the intrinsic properties of materials involved, which hinders the quick optimization of the LIB electrodes and PEMFC GDLs manufacturing processes.[24,25] Additionally, experimental outputs have limited resolution, and often it is difficult to characterize and track the microstructure formation process over time, thus limiting the way researchers can control and optimize experiments. To compensate the intrinsic experimental limitations, computer simulations arose as efficient complementary tools to assess LIB cell processes and GDL performance.[26–29] Computational modeling allows to understand LIB cells process from a different perspective by resolving numerically the mathematical equation that describes the physical process taken under consideration.

In the case of LIB cells manufacturing, the ARTISTIC project[30] has been a pioneer in optimizing these processes with different computational modeling techniques at the mesoscale. The ARTISTIC project simulates the entire manufacturing chain of electrode and cell, from the slurry preparation, passing by its drying, its calendering, its electrolyte filling, to reach the resulting cell performance. These physics-based computational models simulate and predict the influence of materials properties and manufacturing parameters on the electrode and cell properties.[16] They have been calibrated and validated against experimental data. To face the computational cost that these models can have, data-driven Machine Learning (ML) surrogate models have also been trained with the physics-based models obtained datasets to accelerate the optimization of different manufacturing aspects.[24,25,31,32] Recently, in the LIB cell field, a Deep Learning (DL) model has been trained to track microstructure evolution over time during the electrode calendering by using Discrete Element Method (DEM) time series data. [33] Also, for PEMFCs, Random Forest (RF) models have been trained to predict different properties of the GDLs as a function of their most relevant manufacturing parameters.[34]

Since the numerous variables impacting the final electrode quality and performance, optimizing these processes with, for example, a trial-and-error method is not straightforward. In this scenario, ML techniques are excellent tools to unveil patterns and relationships hidden in this data and to optimize these processes.[35] ML algorithms have a huge potential in other critical domains, including applications such as material discovery, real-time monitoring, state estimation, battery usage, fault detection or life cycle management.[36] As we have previously demonstrated in our ARTISTIC project initiative, ML can be used to accelerate both the understanding of new materials (chemistry and formulation), and the optimization of LIB electrode and cell manufacturing process.[37]

Within ML, supervised ML techniques require labeled data, where each input data point has an associated output value, to enable data-driven predictions and optimizations. On the other hand, unsupervised ML uses unlabeled data to find patterns in it. For LIB cells, both mentioned types of ML algorithm have been applied to experimental datasets. Particularly for NMC electrodes, we have studies involving different stages of the manufacturing chain with different algorithms. For example, Pinto-Cunha *et al.* analyzed Decision Trees (DTs), Support Vector Machine (SVM), and Deep Neural Networks (DNNs) algorithms to uncover the interdependencies between slurry parameters and NMC final properties.[38] Duquesnoy *et al.*, in addition to considering slurry parameters, included coating ones to develop an automatic methodology that used a Gaussian Naives Bayes classifier to determine if the resulting electrode is homogeneous or heterogeneous.[31] Furthermore, K-Means clustering was used in the calendering step of NMC-based electrodes by Primo *et al.*.[39] For graphite anodes, Faraji-Niri *et al.* collected a lab-scale dataset containing control variables in the slurry and coating stages to predict final properties of the electrode through the use of RF models.[40] For the State of Health (SoH) estimation of commercial LGM50 cells, a Gaussian Process Regressor was trained by Faraji-Niri *et al.* by selecting features of electrochemical impedance spectroscopy (EIS) data.[41] Moreover, Neural Networks (NNs) have been developed to detect cracks in LIB electrodes by using 3D image data[42] and to map the 3D architecture of NMC particles with focused ion beam slicing in sequence with electron backscatter diffraction data.[43] Meanwhile for GDLs, various literature works show the use of ML models for different applications. For instance, Hou *et al.* formulated an Extreme Learning Machine (ELM) model that allowed to obtain the optimal GDL structure parameters with the minimum temperature, maximum current density, and good oxygen concentration uniformity.[44] Shum *et al.* used DT and convolutional NN (CNN) algorithms to segment GDL’s X-ray computed tomography (CT) image stacks, comparing their performance with basic image processing techniques.[45] In addition, Cawte *et al.* developed a 3D CNN to predict the GDL materials’ permeability directly from 3D binary image data.[46] While Froning *et al.* also used a CNN model to predict the GDL materials' permeability, but with stochastically generated microstructures.[47] Saco *et al.* tested and observed SVM regression, Linear Regression (LR) and k-Nearest Neighbors algorithms on different humidification processes during experimental studies of PEMFCs. They concluded that, in their case of study, LR provided better accuracy that other models.[48] Furthermore, for deformed GDL, Wang *et al.* Built an M^5 model, which includes multi-physics and multi-phase flow simulation, ML-based surrogate modelling, multi-variable and multi-objects optimization. They also compared response surface methodology (RSM) and artificial NN (ANN) methodologies. This M^5 model proved to be effective and efficient for optimizing the GDL current density and oxygen distribution.[49] It is worth mentioning that all these previous works have emphasized the development of ML tools to analyze vast datasets. Surprisingly, none of the previous works addressed the problem of how to derive reliable ML models with smaller datasets, arising either from the lack of enough experiments or from the computational cost of running large simulations.

Transfer Learning (TL) is a very interesting paradigm within ML that takes advantage of the knowledge learnt from solving one task to accelerate learning and improve performance on a related but distinct task. This approach uses some existing ML model trained on a vast dataset in the source domain and adapts or extends it to extrapolate its predictive power to a different domain with a smaller target dataset. This significantly reduces training time and data requirements compared to building a model from scratch. TL practices are usually linked to NNs that allow data-driven strategies to benefit from existing knowledge in related domains, improving their overall performance. TL has proven excellent results in different fields, such as medicine, mechanics, arts, physics, security or biology.[50] Specially in tasks which involve computer vision[51,52] and natural language processing techniques.[53,54] TL has also been used in LIBs electrode and PEMFCs research, particularly for battery state estimations and ageing prognostics, extrapolating predictions to different domains and usage conditions.[55–59] As far as we know, TL has not been used in LIBs cell or PEMFC GDLs manufacturing at the time of this writing.

There are four main approaches for transferring knowledge: feature-based, instance-based, parameter/model-based and relational/adversarial-based.[50,60] By adjusting the weights of individual instances (data points), instance-based transfer bridges the gap between the source and target domains, even when the overall data distributions differ. Feature-based transfer focuses on transferring the feature representation learned from the source domain to the target domain, while parameter-based transfer directly transfers the weights and biases learned by the pre-trained model as a starting point for the target domain model. In NN models, this approach freezes some layers and/or finetunes layers and/or adds some fresh layers to the original model. Finally, relational-based TL approaches transfer logical relationships or rules learned from the source domain to the target domain and are usually connected to generative adversarial networks (GANs).[51–56,60]

In this present work, we propose a simple TL approach to understand how relationships between manufacturing parameters and electrodes properties can be transferred to different chemistries with experimental data and to different volume sizes with stochastically generated data (Figure 1). This proposed TL approach allows dealing with small datasets, which is commonly the case in academic research laboratories. In the experimental demonstration, we use a larger Graphite dataset to train a NN and transfer it to Si-Gra and NMC smaller datasets. In the case GDLs, we use a small volume dataset with lots of calculation to train a NN and transfer it to a larger volume dataset with less calculations that are computationally more expensive. It can be highlighted that none of these datasets were specifically generated with the purpose of training a ML model. Therefore, its distributions are not homogeneous, but our approaches herein allow us to obtain good results even with this aspect, which shows the robustness of the method. In the following Section, we explain our findings in applying these approaches to our manufacturing process experimental dataset on LIBs cells and stochastically generated dataset on PEMFCs. We also use Explainable Artificial Intelligence (XAI) to interpret the behavior of our NN's predictions, before and after TL approach being applied. Finally, we conclude with a discussion of the results obtained and indicate the future perspectives for our work.

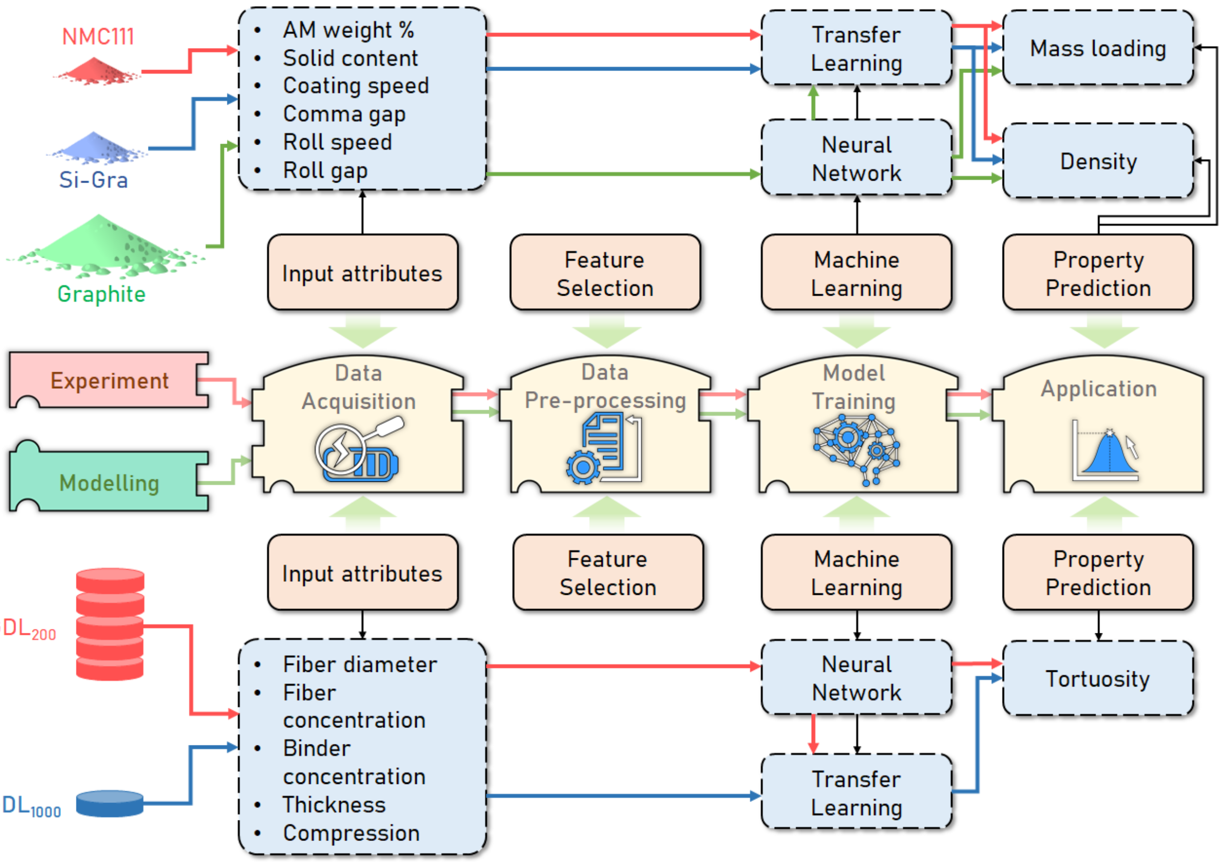

Figure 1. Our workflow for the application of the simple Transfer Learning (TL) approach. In the upper part of the diagram, we have the case of applying it to an experimental dataset to predict electrode density and mass loading using Graphite data as the vast data source and transfer it through the TL approach to Si-Graphite (Si-Gra) and NMC smaller datasets. In the lower part of the diagram, we have the case of applying to modelling dataset (GDL$_{200}$ as a source dataset and GDL$_{1000}$ as target dataset, explained in the Methods section) to predict geometrical tortuosity.

Results

Experimental LIB cell manufacturing dataset

Overall, our pre-existing experimental dataset consists of 235 graphite-based, 53 Si-Gra-based and 63 NMC-based electrodes that were fabricated with the conditions specified in the Methods section. Figure 2 shows the distribution of the experimental manufacturing parameters for each chemistry. As global aspects of this distributions we can highlight that Graphite is the most extensive one, in what respects to the range of values considered and amount of data that can be appreciated in the counts *y*-axis. Then, Si-Gra and NMC have parameters in the same range except for some cases like the AM weight percentage in Si-Gra or solid content also in NMC. This makes the decision to use TL a good choice since it is expected that the extra layer will adapt the model to each of these particularities. The goal of this work is to learn the impact of these six input features on final electrode properties from Graphite-based electrodes and then transfer this learning to Si-Gra- and NMC-based electrodes. The size of these datasets reflects a typical experimental case where the acquisition of them demands a lot of resources. So, the simple TL approach proposed here is aimed at this kind of case recurrent in academic laboratories.

The AM weight percentage varies from 85 % to 97.5 % percent for NMC and from 91 % to 95.5 % for graphite, this reflects the electrode density of commercial cells. While for Si-Gra the AM weight percentage corresponds to the weight percentage of Si in Graphite and goes from 8 % to 15 %. A coating speed value of 0.3 m/min is considered for Graphite and Si-Gra, while for NMC there are more cases considered between 0.2 m/min and 1 m/min. Regarding comma gaps, the range of values goes from 100 to 300 µm for graphite and Si-Gra electrodes and from 50 to 400 µm for NMC electrodes. The values of the roll gap have been previously calibrated to produce different pressures for different values of the calendering gap.[39, 61] For example, Primo et al. from our group calibrated the dependence of the pressure with the roll gap for a given electrode.[49] While for Graphite the minimum and maximum values are 1 µm and 135 µm, for Si-Gra and NMC these values are 15 µm and 102 µm, and 20 µm and 206 µm, respectively. And their respctive mean values are 70 µm, 58 µm and 62 µm. For the roll speed we have two possible values of 0.27 m/min and 0.54 m/min. Finally, the solid content varies from 42 % to 66 % for NMC and from 22 % to 42 % for Graphite slurries, since the graphite slurry is more viscous at the same shear rate and formulation[62,63] due to the choice of the binder, and the solid content for Si slurries are close to the lower values of graphite (from 24 % to 32 %).

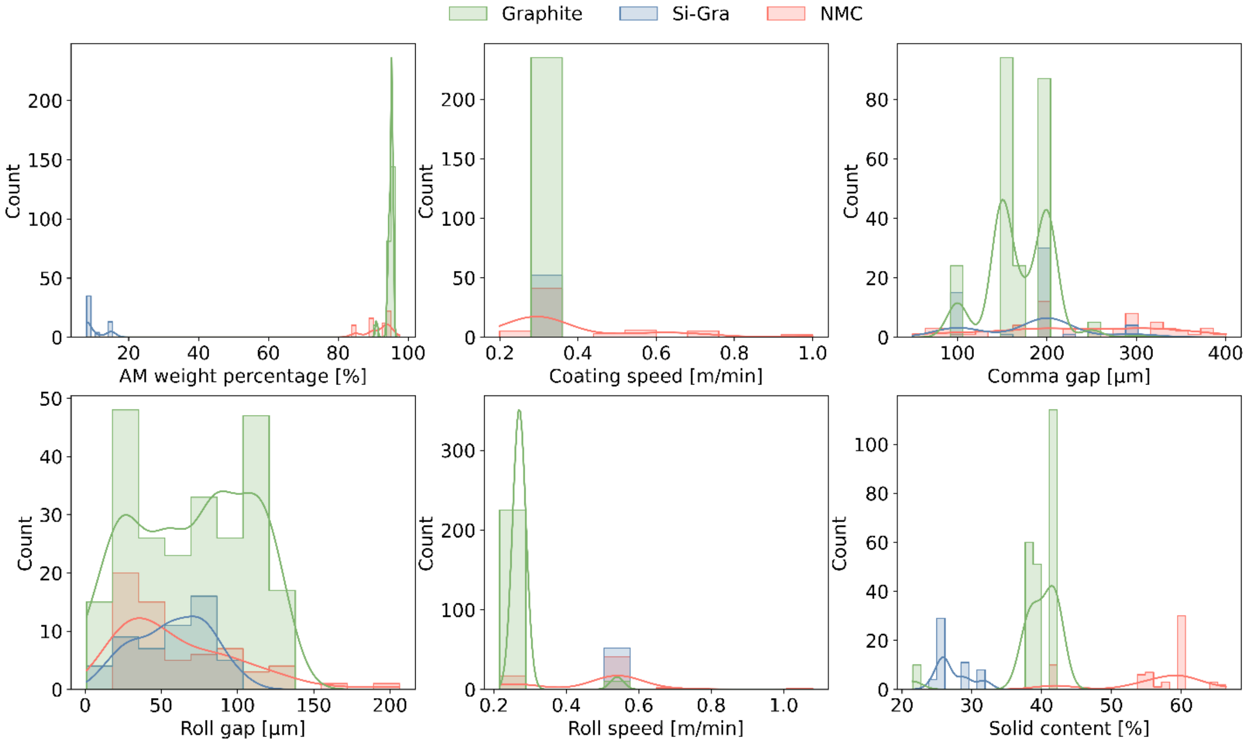

Figure 2. Distributions of the pre-existing experimental dataset manufacturing parameters used as input features in the feed-forward NNs for each electrode chemistry: Graphite (green), Si-Gra (blue) and NMC (red).

The final electrode properties considered in this work to predict are density and mass loading, which their distributions are presented in Figure 3. Electrode density together with the electrode mass loading are important properties that control the final performance of the LIB cells. Higher electrode mass loading and electrode density leads to a higher energy density with a trade-off of a lower power density. The optimization of these properties is always a balancing act and is also highly dependent on the type of electrode. As we can see in Figure 3a, Graphite- and Si-Gra based electrodes are generally less dense than NMC-based electrodes due to the lower density of graphite, which determines the maximum density of the final electrode density. On Figure 3b, the mass loading of NMC-based electrodes is wider and considers larger values than the other two AMs. The higher mass loading is due to two factors. NMC has a higher density than graphite, resulting in a higher mass of AM in the same volume of the electrode. Also, as the solid content of NMC slurry phase is higher, a higher volume fraction of NMC is on the same area of the current collector for the same comma gap compared to Graphite or Si-Gra, resulting in a higher mass loading of NMC electrodes compared to those other electrode chemistries.

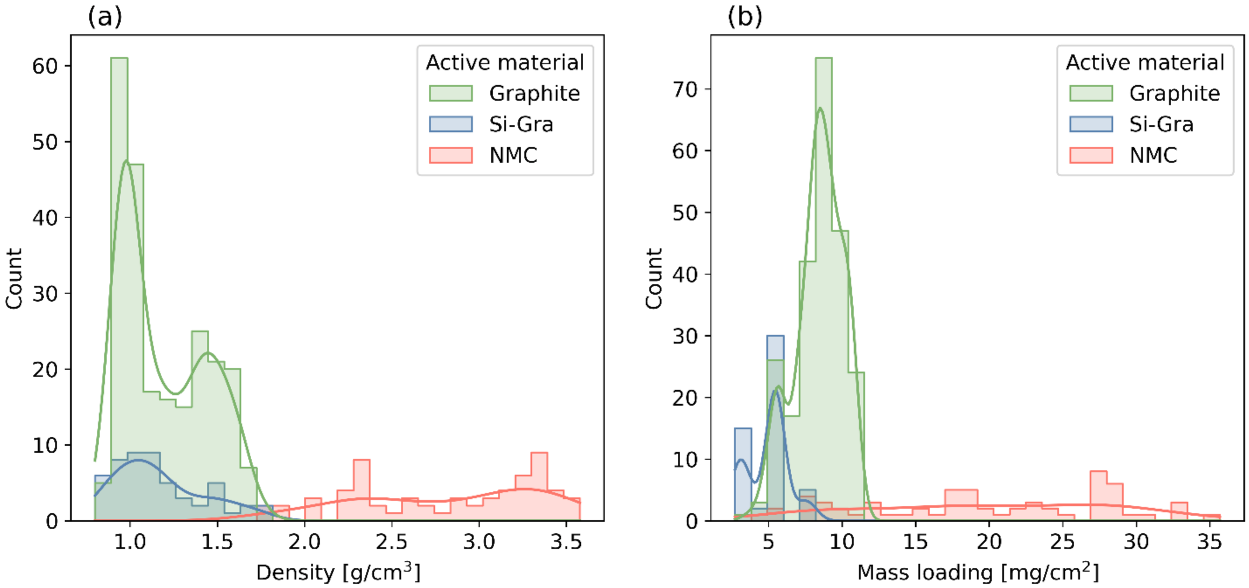

Figure 3. Distributions of the targets electrode properties for the feed-forward NNs: (a) Density and (b) Mass loading. In each plot the electrode chemistries are represented with the following colors: Graphite (green), Si-Gra (blue) and NMC (red).

In this experimental demonstration of our simple TL approach, we studied the dependence of electrode density and mass loading on the fraction in mass of AM and percentage of solid content in the formulation; coating speed and comma gap during coating; and roll speed and roll gap during calendering. To simplify the posterior application of TL techniques and training, we separated the two prediction problems, *i.e.* prediction of electrode density and prediction of mass loading. In both cases, a train-test split of 70 %-30 % was performed on the dataset per electrode. Then, 10 % of the training set is separated as validation set during the training. The optimization loss function was the Mean Absolute Percentage Error (MAPE) and the Adam optimizer was used per 250 epochs. Figure 4 shows the MAPE loss of the NN with the Graphite dataset for both cases of density and mass loading. For both models, it can be seen that the loss decreases with an asymptotic shape until it reaches a plateau for both train and validation sets. This indicates that optimal weights of the NNs are found and there is neither over- nor under-fitting. The following results in plots and tables correspond to evaluations in the test set.

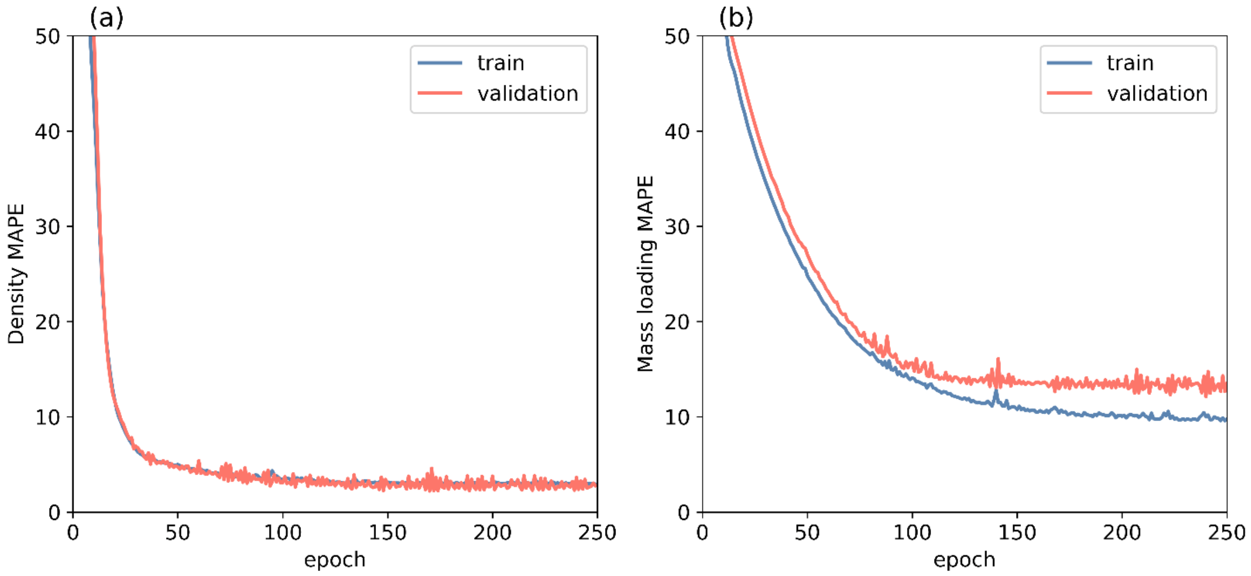

Figure 4. Mean Absolute Percentage Error (MAPE) loss plot for (a) Density and (b) Mass loading for both training (blue curve) and validation (red curve) Graphite datasets when training with the NN model.

Having obtained the good performance of the NNs for graphite, that could capture the relationships between the experimental features and targets, now we extend it to Si-Gra and NMC smaller datasets. Training this kind of model for both of these electrodes with the lack of data leads to overfitting in the respective training set, as shown in Figures S1 and S2 of the Supporting Information and the discussion there. Thus, the aim of this section is to adapt these NNs with the proposed TL approach to the new chemistries. To overcome this problem, we freeze the weight in the architecture connections of the NN for graphite and add an extra hidden layer to each one of the other chemistries with the same number of nodes in the corresponding architecture. So, being only the weights of this layer trained the problem adapts better to the amount of data of Si-Gra and NMC. The need for these additional layers can be justified with the results shown in Table 1. The pre-trained NN for predicting electrode density gives an error of 4.53 % when evaluated with graphite-based test data. The error of this model increases up to 78.81 % and 56.13 % when tested on Si-Gra and NMC test data. This is because the pre-trained model is extrapolating outside the feature range for which it was fitted, as seen in Figures 2 and 3. In the next row of Table 1 it can be appreciated a diminution in both Si-Gra and NMC errors, where these errors decrease to 14.53 % and 8.09 %, demonstrating the improvement of the TL approach NN when an extra layer is added. For the NNs to predict electrode mass loading we have a similar behavior being 13.9 % the error when evaluated in graphite test data and increasing to 44.98 % and 70.82 % for Si-Gra and NMC data, respectively. These errors decrease to 3.71 % and 10.61 % after the simple TL approach is applied.

Table 1. Mean Absolute Percentage Error (MAPE) of density and mass loading predictions in the test sets for both, pre-trained and TL approach NNs.

	Error (MAPE) [%]					
	Density			Mass loading		
	Graphite	Si-Gra	NMC	Graphite	Si-Gra	NMC
Pre-trained NN	4.53	78.81	56.13	13.90	44.98	70.82
TL approach NN	--	14.53	8.09	--	3.71	10.61

Figure 5 shows this in a more graphical way, where individual predictions are plotted against its actual value. In general aspects, in the left column of plots we have the pre-trained NNs, so with the results of the MAPE presented in Table 1, a good performance is not expected Si-Gra and NMC test data. In the right column we have the transferred NNs, so an improvement is expected with respect to the left column. Figures 5 show the linear tendency of an ideal model as a dashed gray line. For both pre-trained NN (Figures 5a and 5c), the predictions of Graphite are displayed, where in the case of density we obtain a good behavior while for the case of mass loading an artifice of overestimating low mass loading values is generated. Both Si-Gra and NMC are underestimating the actual values for the density and overestimating the Si-Gra mass loading. In Figure 5b and d it is shown how this is fixed with the TL approach NNs, where Si-Gra and NMC predictions are improved in the range of expected values, despite the relative differences between them are not modified in the density prediction but they are improved for the mass loading predictions, where even the tendency slope is improved for both chemistries. Thus, the simple TL approach allowed us to generate new models with great accuracy despite the limitation in the size of the data.

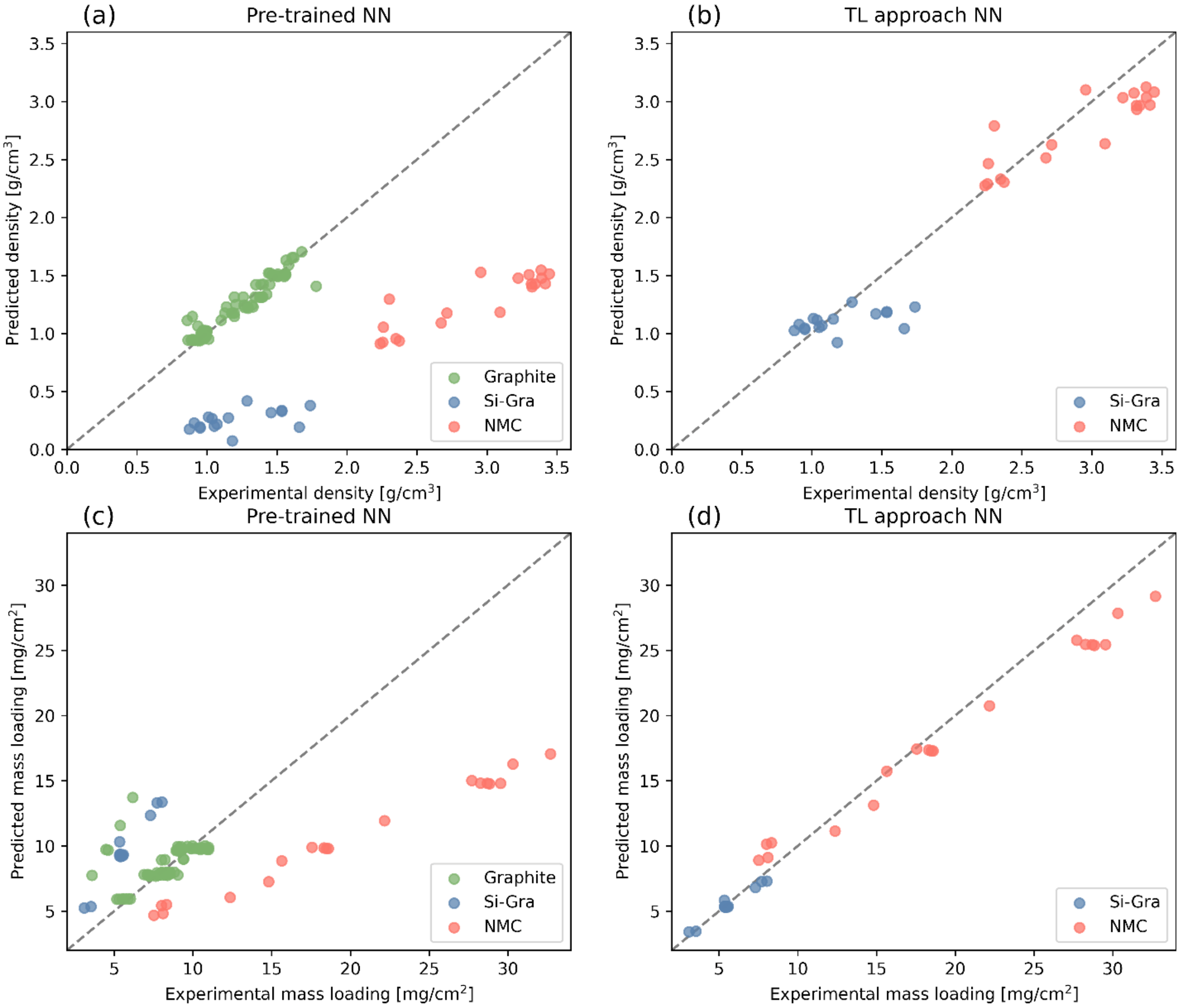

Figure 5. Prediction versus experimental values of: (a) Density (Pre-trained NN), (b) Density (TL approach NN), (c) Mass loading (Pre-trained NN) and (d) Mass loading (TL approach NN) in the test sets. In each plot the electrode chemistries are represented with the following colors: Graphite (green), Si-Gra (blue) and NMC (red).

To add explanation to the predictions of the NNs, we use XAI, which is a technique used in AI to add interpretability and transparency to the usual black-box ML models. In Figure 6 we show the Shapley values for the pre-trained and the TL approach NNs for a randomly selected test experiment for each chemistry. These Shapley values compute the importance of each feature close to a fixed data point when all the other feature values are constant.[64] This allows us to compare the impact of each manufacturing parameter on the final electrode property for the different chemistries when evaluating a given experiment. The base value indicates the average of all predictions in the dataset of the given chemistry. The red or blue color of the arrows in these plots indicates whether the associated feature, with the specified value and unit, pushes the prediction to a higher or lower value relative to this base value. The magnitude of each feature's contribution is indicated by the size of the corresponding arrow. When all these arrow lengths are added to the base value, with the respective sign given by the color, the final prediction is obtained. For the selected experiment with Graphite, we have a major impact of the AM wt.%, roll gap and the comma gap by pushing the prediction to the negative side of the base value, while the solid content pushes it to the positive side. While for the selected experiments of Si-Gra and NMC, the influence in their prediction is dominated in both cases by the roll gap, comma gap and the AM wt.%, with same direction on each one but with different intensities. This XAI allows the further improvements of these specific experiments by indicating which manufacturing parameters have more influence in the electrode property.

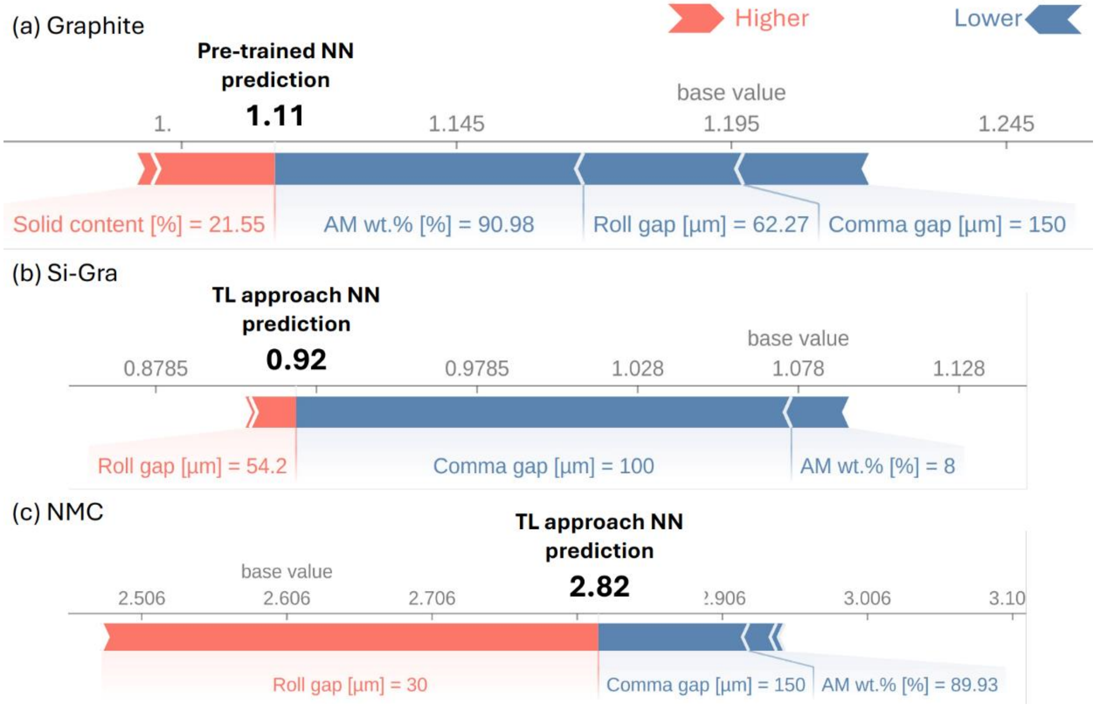

Figure 6. Representation of Shapley values for the prediction of the NN for electrode density for: (a) Graphite, (b) Si-Gra, and (c) NMC active materials. These plots show how the input features of a specific data point contribute to the NN's prediction, by showing the magnitude and direction of the contribution as arrows with different colors for increase (red) or decrease (blue).

To have a global overview of the importance of each manufacturing parameter in the prediction of density, we summarize in Figure 7 the evaluation of Shapley values for each experiment in the test sets. Here each dot is a particular experiment of the experimental dataset. For Graphite experiments, pre-trained NN was used, while for Si-Gra and NMC, the respective TL approach NNs were used. The color of each dot indicates the value of the feature (relative to its distribution) while the *x*-axis positions indicate the individual impact in the NN prediction (SHAP value). The *y*-axis of each subfigure is sorted in descending order of importance of each manufacturing parameter. We can highlight that the impact of the manufacturing parameters on the NNs prediction depends on the chemistry. This particularity indicates that the TL approach can modify the relevance of the manufacturing parameters in the pre-trained NN when transferred to a new dataset. While for Graphite and Si-Gra pre-trained and TL approach NNs, respectively, the manufacturing parameters that have a larger influence in the outputs are roll gap, comma gap, AM wt.% and solid content. For the NMC TL approach NN, the three most relevant manufacturing parameters change their order with respect to the previous ones: comma gap, roll gap, and AM wt.%. It can be highlighted that in all cases roll speed and coating speed do not have an impact in the NN's predictions. This can be attributed to their distributions (see Figure 2), which are composed of specific values. This should not be misunderstood as meaning that these manufacturing parameters have no impact in the final electrode properties, but as a characteristic of the trained NNs with the particularities of the pre-existing experimental dataset. Moreover, this global representation could be used for selecting features and considering a less complex model without taking into account these manufacturing parameters for this case or to improve their experimental sampling.

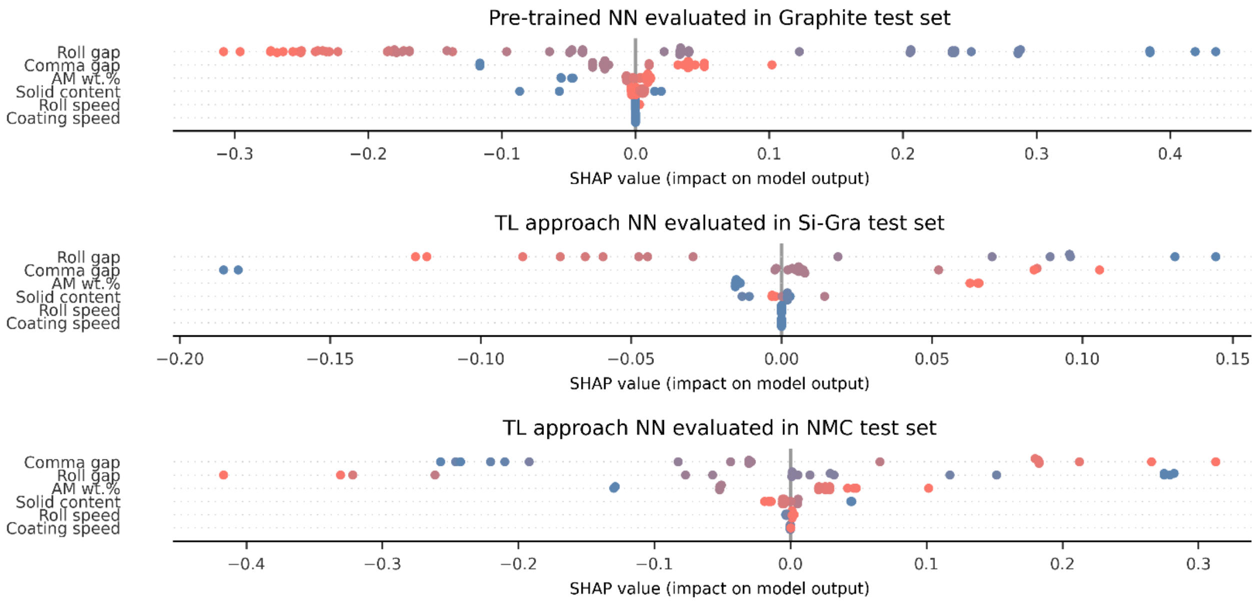

Figure 7. Global representation of Shapley values for the predictions of the NNs for electrode density for: (a) Graphite, (b) Si-Gra, and (c) NMC AMs. The SHAP value of each manufacturing parameter for each test experiment is given in the *x*-axis, while the color of each dot indicates if the feature value is higher

(red) or lower (blue), relative to its distribution. The *y*-axis is sorted in descending order per manufacturing parameter relevance for the NN.

Stochastically generated GDL manufacturing dataset

The overall performance of the proposed TL approach might not be perfect, considering the percentage errors for some cases presented in Table 1. Nevertheless, this could be attributed to the particular distribution of the pre-existing experimental dataset. That is where our stochastically generated GDL manufacturing dataset comes into the picture. The source GDL_{200} dataset has 240 entries, while the target GDL_{1000} has 78 entries. These sizes maintain a similar relationship between source and target datasets sizes of the experimental demonstration. But, since these are stochastically generated, they have a more homogeneous distribution. Despite the improvement in this aspect, these data were not specifically generated for the purpose of demonstrating this TL approach, which makes the results obtained even more robust. The distribution of the input features for the NN to predict the geometric tortuosity are shown in Figure S3. In the GDL_{200} dataset, a uniform distribution is presented. While the GDL_{1000} presents some particularities due to the smaller amount of data. For both datasets we have similar ranges for every input parameter. Fiber diameter ranges from 6.0 to 12.0 µm. Fiber and binder concentrations vary from 10% to 25% and from 5% to 10%, respectively. The thickness goes from 280 to 320 µm, and, finally, the factor compression from 0.0 to 0.5.

The distributions in each dataset of the geometrical tortuosity are shown in Figure 8, which is the target predicted by the NN in this section. The geometric tortuosity of the GDL is an important property as it plays a crucial role in gases, liquids and heat transport within the system. It also affects the permeability, which ultimately impacts the efficiency and performance of the PEMFC. Higher tortuosity means longer diffusive paths, which will affect the GDL's transport properties. It can be highlighted that both GDL_{200} and GDL_{1000} geometrical tortuosity are right-skewed distributions, and GDL_{1000} is shifted to the right of the

GDL_{200} one. While the mean value of the GDL_{200} is 1.07, the GDL_{1000} is 1.09. Also, the minimum value in GDL_{200} is 1.03, while in GDL_{1000} is 1.08. Both of the distributions extend till 1.17.

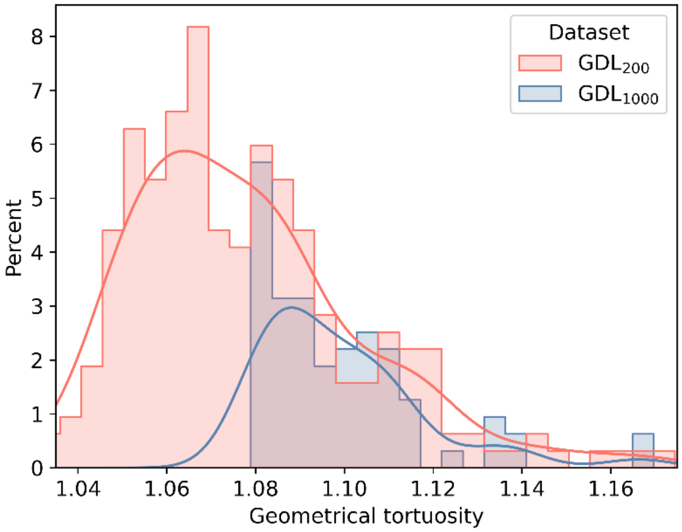

Figure 8. Distributions of the target geometrical tortuosity for the feed-forward NNs for each dataset: GDL_{200} (red) and GDL_{1000} (blue).

For the training of the NN, a train-test split of 70 %-30 % was performed on each dataset, being the first one only used in the training and the second one for the test evaluations performed in the following tables and plots. As in the previous case, the optimization loss function was the MAPE, and the Adam optimizer was used per 250 epochs. Figure S4 shows the MAPE loss of the NN with the GDL_{200} dataset, where the loss decreases with an asymptotic behavior and reaches a plateau close to 2%. When this NN is evaluated in the test sets, we have a MAPE value of 2.13% for GDL_{200} and of 2.61% for GDL_{1000}. This higher error for GDL_{1000} can be improved by applying the TL approach that already showed improvement in with the experimental dataset. By adding and training the extra layer to the pre-trained NN, then the evaluation in the GDL_{1000} test set decreases to 1.96%. This information is summarized in Table 2, demonstrating that there is also an improvement with the TL approach when applied to this stochastically generated dataset.

Table 2. Mean Absolute Percentage Error (MAPE) of geometrical tortuosity predictions in the test sets for both, pre-trained model and TL approach.

Geometrical Tortuosity MAPE [%]		
	GDL_{200}	GDL_{1000}
Pre-trained NN	2.13	2.61
TL approach NN	--	1.96

Individual predictions are plotted versus the target values for the GDL_{1000} test set and both pre-trained (red squares) and TL approach (blue circles) NNs in Figure 9. As expected with the values of Table 2, the predictions of the pre-trained NN have a higher scatter in the predicted *y*-axis. This scatter is improved with the TL approach NN by having each prediction closer to the ideal prediction line. This improvement is clearer in the range that goes from 1.08 to 1.12, the three cases with higher geometrical tortuosity are worsened. However, these values are in the tail of the distribution, being less sampled than the ones in the range that is improved.

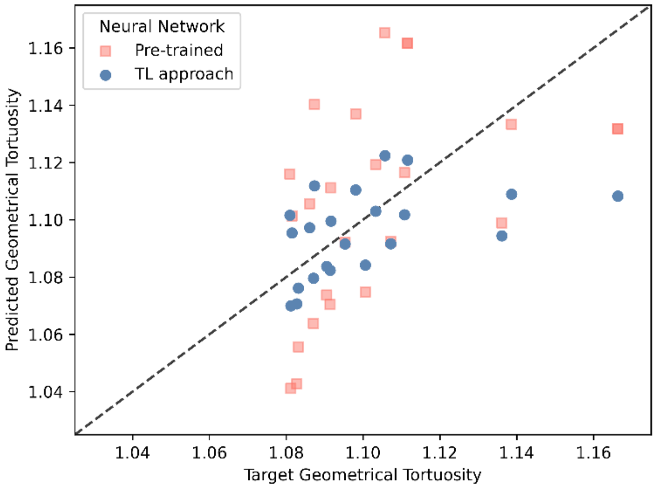

Figure 9. Predicted versus target values of Geometrical Tortuosity in test set of the GDL_{1000} dataset with the pre-trained NN (red squared) and with the TL approach NN (blue circles).

Finally, we also use XAI in these datasets where entries of the GDL_{200} and GDL_{1000} test sets are randomly selected and evaluated with the pre-trained and the TL approach NNs, respectively. The obtained Shapley values are displayed in Figure S5. In the first case we have a major influence in the negative direction, relative to the base value, that it is mandated by thickness, fiber concentration and fiber diameter. While compression and binder concentration have similar contributions but in the opposite direction. For the second case compression is the only parameter that pushes the prediction to the negative direction. While all the other parameters push it to a higher value, thickness and fiber concentration being the most relevant ones for this test example. Going further, we can replicate this analysis for all the samples in the respective test sets and evaluated with the respective NNs. If this information is plotted together (Figure S6), we get an overview of the influence of each feature in the NNs predictions. In these stochastically generated GDL datasets we get that the influence of the features both in pre-trained and TL approach NN are in the same order of importance, *i.e.* there is not a significant change in the relative importance of each feature to the others when the predictions are made. As can be seen in Figure S6, the order of the importance of the features is the following one: thickness, fiber concentration, binder concentration, fiber diameter and compression. Thickness is the most relevant one and compression is the least relevant one in determining the geometrical tortuosity of the GDL microstructure datasets with our pre-trained and TL approach NNs.

Discussion

The novel and simple TL approach proposed in this work has proven to be suitable for EEC manufacturing problems. It was demonstrated with pre-existing experimental and stochastically acquired datasets. The well performance obtained for both cases reflects the robustness of the method by not considering datasets specifically designed with the purpose of training ML models. In every case, the interpretation of the models' predictions and the importance of each feature was explained by XAI.

In the first application, the experimental dataset consisted of manufacturing process data of LIB cells with different AM chemistries. The approach consisted of using a vast Graphite dataset to train NNs to predict electrode density and mass loading. These NNs were trained using as feature the following manufacturing parameters: weight percentage of AM and solid content in the formulation, coating speed and comma gap during coating, and roll speed and roll gap during calendering. The architecture of the NNs was designed differently for each target property. These NNs performed well in the Graphite dataset, but their performance metrics diminished when used to extrapolate in the smaller datasets of Si-Gra and NMC. The distribution of these Si-Gra and NMC datasets had both similarities and differences with the Graphite dataset, but they were not large enough to train NNs from scratch. This justified the use of TL by adding an extra layer to each one of the Graphite pre-trained NNs and training this extra layer to adapt these models to each one of these new chemistries. In both cases, the performance of the evaluation metrics improved considerably when evaluated with the TL approach NNs predictions. The interpretation of the influence of each parameter in the NNs predictions was also discussed for some test experiments for each chemistry using XAI. The global analysis of Shapley values allowed us to determine the influence of each feature on the final predicted properties and sorted them by relevance, showing that this depended on the type of chemistry.

The second application of the simple TL approach was in the context of PEMFCs with stochastically generated GDL datasets with different volume sizes. In this case, small volume microstructures with lots of calculations were used to train a NN to predict the geometric tortuosity considering as input parameters the fiber diameter, the fiber concentration, the binder concentration, the thickness, and the compression. Then, the NN was transferred to a smaller dataset with microstructures of larger volume that were computationally more expensive to characterize. Since these datasets were stochastically generated, they have a more homogeneous distribution than the experimental ones. This property in the data resulted in even better results, which proved that the simple TL approach can perform better when applied to better distributed datasets.

This work provides a proof-of-concept for developing efficient data-driven models with the simple TL approach to predict final electrode properties for new chemistries or high simulation volume sizes, by taking advantage of pre-trained NNs when available data is not enough (as it can happen in academic laboratories). Our work perspectives include the application of our approach to LIB electrode formulations with other chemistries and to Sodium Ion and Solid-State Battery electrode manufacturing processes. We believe that the proof-of-concept presented in this article illustrates that simple AI approaches can still deliver a lot in the complex field of EEC manufacturing.

Methods

Sample preparation and properties measurement in LIBs

Our pre-existing experimental dataset consisted of three different chemistries for the LIB electrode AM: Graphite, Si-Graphite composite (referred to as Si-Gra) and NMC. It is worth mentioning that it was not acquired with the purpose of demonstrating the TL approach proposed in this work. For the positive electrode, $LiNi_{1/3}Mn_{1/3}Co_{1/3}O_2$ (NMC) AM, supplied by Umicore, was used. C-NERGY™ super C45 carbon black (CB) from IMERYS and Solef™ Polyvinylidene fluoride (PVDF) from Solvay were used as the electronic conductive additive and the binder, respectively. Before mixing with the solvent, the powder components were first premixed overnight in a Turbula® mixer. The mixture was then transferred to a Dispermat CV3-PLUS high-shear mixer and the required amount of NMP (BASF) was added. The resulting mixture was mixed for 2 hours at 25 ^oC and 3000 RPM. For the graphite electrode, Na-CMC (molecular weight ~250 K and degree of substitution ~0.7, Sigma Aldrich), C-NERGY™ super C45 carbon black (CB)(IMERYS), and water were used as the binder, conductive additive, and solvent, respectively. The slurry mixing step was similar to the NMC slurry. For some of these graphite electrodes, Si nanoparticles were also used as AM blended with graphite and denoted as Si-Gra.

The resulting slurries were coated over a copper current collector (16 μm) for Graphite and Si-Gra electrodes and an aluminum current collector (22 μm) for NMC electrodes with a prototype-grade comma-coater machine (PDL250, People & Technology, Korea) at various comma gaps and coating speeds as discussed in the experimental case of the Results. The electrodes were dried in a built-in two-part oven at 80 and 95 °C for NMC electrodes and at 60 and 65 °C for Graphite and Si-Gra electrodes due to the different solvents used. The calendering of the electrodes was done with a prototype-grade lap press calender (BPN250, People & Technology, Korea) at various roll gaps and roll speeds. The temperature of the calendering process was maintained at 60 °C for all the electrodes.

The resulting electrodes were characterized in terms of density and mass loading, providing a measurement of electrode energy density. A sample of electrode sections, 13 mm in diameter, was punched out of the electrode. Resulting electrode section's thickness and mass were measured, subtracting the thickness and mass of the current collector to yield the final mass and thickness of the electrode. Mass loading (m_l) of the electrode was calculated as:

$$m_l \left(\frac{mg}{cm^2}\right) = \frac{f_{AM} \times (m_{el+cc} - m_{cc}) \times 4}{\pi \times 1.3^2} \tag{1}$$

where, m_{el+cc} is the mass of the electrode along with the current collector, m_{cc} is the mass of the current collector, and f_{AM} is the total fraction of the active materials. The density (ρ) of the final electrode was calculated as:

$$\rho \left(\frac{g}{cm^3}\right) = \frac{m_l \times 0.001}{f_{AM} \times (t_{el+cc} - t_{cc})} \tag{2}$$

where t_{el+cc} is the thickness of the electrode along with the current collector, in cm, and t_{cc} is the thickness of the current collector, in cm.

The formulation of the slurry, the coating and drying process parameters, and the calendering process parameters are taken as the input features of the model. The slurry is mixed at the same mixing speed and for a long enough duration for each type of electrode to ensure a homogenous mixture. For the formulation, the solid content of the slurry and the weight percentage of AM is varied. Equal weight percentage of carbon additive and binder is taken for all the formulations. The solid content of the slurry is defined as,

$$\text{Solid content (\%)} = \frac{\text{dry mass (i.e. mass of AM + carbon additve + binder)}}{\text{dry mass + mass of solvent}} \quad (3)$$

The coating and drying process are performed roll-to-roll. The parameters which control the coating and drying processes are coating gap, coating speed, and drying temperature. Among these parameters, drying temperature is fixed for each type of electrode according to the solvent and the other parameters are varied. Finally, the dried electrodes undergo the calendering process which is controlled by the roll speed, the roll gap and the roll temperature. In our experiments, the roll temperature is fixed, and the roll gap and roll speed are varied. The fixed parameters for the mixing process were chosen given previous optimizations already performed in previous publications of our research group.[39,65] The experimental dataset used in the current work was obtained and collected under the context of the ARTISTIC project.[30]

Stochastic Generation of GDL microstructure and calculation of geometric tortuosity

The GDL microstructures were generated using the FiberGeo module within the Geodict[66] software. The microstructures were stochastically generated and digitally characterized along with other properties in the context of our previous work[34]. In this work, geometric tortuosity was not used to train any ML model. The microstructures there consisted of infinite/ circular carbon fibers with the specified solid volume percentage (%). We used it here with domain sizes 2000 μm × 200 μm × thickness μm and 1000 μm × 1000 μm × thickness μm with a voxel length of 1 μm. These domain sizes datasets are denoted as GDL_{200} and GDL_{1000}, respectively. Our target property in this case is the geometric tortuosity, which digital characterization in the GDL_{200} dataset takes 65% less computational time than in the GDL_{1000} one. The input parameters to compute this target are the fiber diameter, the fiber concentration, the binder concentration, the thickness, and the compression.

The mentioned carbon fibers have specified diameter and an isotropic orientation using an orientation tensor that can be explained as follows. Mathematically, $\mathbf{d_k} = \begin{pmatrix} x_k \\ y_k \\ z_k \end{pmatrix}$ is the unit vector describing the $\mathbf{K^{th}}$ fiber and $\mathbf{n}$ is the number of fibers. The orientation tensor can be expressed as the sum of the dyadic products of $\mathbf{d_k}$ from all $\mathbf{n}$ fibers, divided by $\mathbf{n}$:

$$\mathbf{T} = \frac{1}{n}\left(\sum_{k=1}^{n} \mathbf{d_k}\mathbf{d_k^T}\right) = \frac{1}{n}\sum_{k=1}^{n} \begin{pmatrix} x_k x_k & x_k y_k & x_k z_k \\ y_k x_k & y_k y_k & y_k z_k \\ z_k x_k & z_k y_k & z_k z_k \end{pmatrix} = \begin{pmatrix} t_{11} & t_{12} & t_{13} \\ t_{21} & t_{22} & t_{23} \\ t_{31} & t_{32} & t_{33} \end{pmatrix} =$$

$$\begin{pmatrix} 0.4966 & 0 & 0 \\ - & 0.4966 & 0 \\ - & - & 0.0068 \end{pmatrix} \qquad (4)$$

Where the diagonal elements define the orientation strength for the corresponding directions. After the generation of carbon fibers, the binder (PTFE) was then incorporated into the GDL domain with the desired solid volume percentage. The Geometric Tortuosity (τ) was then computed to characterize the GDL microstructure. The calculation of geometric tortuosity was conducted in the direction perpendicular to the direction of the carbon fibers using the following equation:

$$\tau = \frac{\text{shortest path to inflow plane}}{\text{distance to inflow plane}} \qquad (5)$$

Transfer Learning Approach

In our approaches herein, we use supervised ML by training feed-forward NNs to the pre-existing data collected from the LIBs cell experiments and the data stochastically generated for GDL, detailed in previous respectively subsections. NNs are selected due to their equation complexity that can learn the underlying non-linear relationships between the manufacturing features and targets. Considering that they also present some limitations, their complex structure can make them prone to overfitting if not carefully regularized and training them often requires large datasets and significant computational resources. To learn the weights of the NNs during training, the Backpropagation algorithm is used.[67]

As shown in the schema in Figure 10, we train a feed-forward NN on the source dataset (Graphite chemistry in LIBs cell experimental dataset and GDL_{200} in stochastically generated dataset) for predicting a final electrode property (density and mass loading in one case and geometrical tortuosity in the other). This NN captures the variations in manufacturing conditions and the changes produced in the target property. For the target dataset (Si-Gra and NMC on one side and GDL_{1000} on the other), we freeze this pre-trained NN (Figure 10a) and add an extra layer to train and perform the same task (Figure 10b). The new layer added for each transferred NN is an adapter, processing the output data and extracting additional features specific to the different manufacturing conditions in the target domain. Thus, adding this extra layer to handle different manufacturing conditions most closely aligns with parameter-based TL. It does not directly modify the input features like the standard feature-based TL where an extra layer is added before the pre-trained NNs, but it also does not directly transfer the pre-trained NN weights (parameters) like parameter-based TL. Instead, it leverages the learned relationships encoded in the pre-trained NN's weights but adapts the final output.

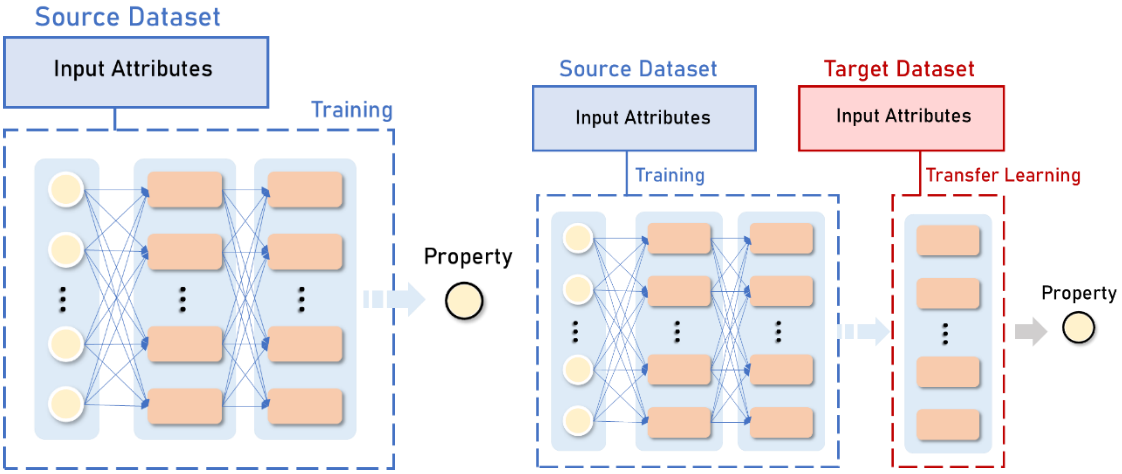

(a) (b)

Figure 10. Training scheme of a feed-forward Neural Network (NN) on (a) source dataset (graphite-based electrodes for LIBs cell experimental dataset, and GDL_{200} for stochastically generated GDL dataset), and then used for a (b) TL approach adding an extra layer for the target dataset (Si-Gra and NMC dataset for LIBs cell experimental dataset, and GDL_{1000} for stochastically generated GDL dataset).

Initially, for the experimental dataset, two feed-forward NNs are trained using the graphite source dataset (pre-trained NNs). One model predicts electrode density, and the other one predicts electrode mass loading. Then, one additional layer is added to each of the pre-trained NNs, creating two TL approach NNs for each output target (electrode density & electrode mass loading). The NN architecture of all the 4 models are depicted in Table 3, where the number of trainable parameters is also specified. For both pre-trained and TL approach NNs we use 6 input parameters: AM weight percentage and fraction of solid (solid content) in the formulation; coating speed and comma gap during coating; and roll speed and roll gap during calendering. In a similar way, a feed-forward NN is trained using the GDL_{200} dataset to predict the geometrical tortuosity by using as input parameters: fiber diameter, fiber concentration, binder concentration, thickness and compression. Then, one additional layer is added to this pre-trained NN to train the TL approach NN in the GDL_{1000} dataset. These other architectures are presented in Table 4. Each hidden layer in all six models is activated with the ReLU function. The codes to train these models were written in Python by using TensorFlow,[68] along with other common scientific computing libraries.[69] They were trained in a 13th Gen Intel(R) Core(TM) i7-13700H with 32 GB of RAM.

Table 3. Feed-forward NN architecture of the pre-trained graphite model, and the TL approach.

Neural Network	Target output	Number of hidden layers	Number of nodes per layer	Total number of trainable parameters
Pre-trained	Density	4	4	93
	Mass loading	3	3	49
TL approach	Density	1 (plus the freezed previous architecture)	4	13

	Mass loading	1 (plus the freezed previous architecture)	3	10

Table 4. Pre-trained and TL approach feed-forward NN architectures for predicting geometrical tortuosity with the GDL manufacturing dataset.

Neural Network	Number of hidden layers	Number of nodes per layer	Total number of trainable parameters
Pre-trained	3	3	46
TL approach	1 (plus the freezed previous architecture)	3	10

Data availability

The datasets used and analysed during the current study available from the corresponding author on reasonable request.

Code availability

The underlying code for this study is not publicly available for proprietary reasons.

Acknowledgement

A.A.F., F.F. and J.F.T. acknowledge financial support from the EU Horizon Europe project DigiCell (Grant Agreement no. 101135486). A.A.F., J.F.T., and D.E.G. acknowledge the European Research Council for the funding support through the ERC Proof-of-Concept Grant No.101069244 (SMARTISTIC project). A.A.F. deeply acknowledges the European Union's Horizon 2020 research and innovation program for funding support through the European Research Council (grant agreements 772873 ARTISTIC project). A.A.F., S.S. and D.E.G. acknowledge the funding support of the French National Research Agency under the France 2030 program (Grant ANR-22-PEBA-0002, PEPR project “BATMAN”). A.A.F. and R.L.O. acknowledge the support of the BLESSED project funded by the European Union under Marie Sklodowska-Curie Actions (Grant Agreement No.101072578). A.A.F. acknowledges the European Union’s Horizon Europe research and innovation program under Grant Agreement No. 101069686 (PULSELiON). A.A.F. acknowledges the Institut Universitaire de France for the support.

Author contributions

FF, JFT, DEG and AAF conceptualized and designed this study. FF, JFT, DEG and AAF established the methodology. SS and RLO curated the datasets. FF and JFT wrote the software code. FF, SS, RLO and DEG made the visualizations and the validation. FF, SS, RLO, JFT and DEG performed the formal analyses. FF, SS, RLO, JFT and DEG wrote the original draft. AAF reviewed and edited the manuscript. AAF acquired the funding and resources for this work, administrated the project and supervised the work. All authors read and approved the final manuscript.

Competing interest

All authors declare no financial or non-financial competing interests.

References

1. Kebede, A. A., Kalogiannis, T., Van Mierlo, J. & Berecibar, M. A comprehensive review of stationary energy storage devices for large scale renewable energy sources grid integration. *Renewable and Sustainable Energy Reviews* **159**, 112213 (2022).
2. Wang, Y., Zhang, X., Li, K., Zhao, G. & Chen, Z. Perspectives and challenges for future lithium-ion battery control and management. (2023).

3. D’Adamo, I., Gastaldi, M. & Ozturk, I. The sustainable development of mobility in the green transition: Renewable energy, local industrial chain, and battery recycling. *Sustainable development* **31**, 840–852 (2023).
4. Mench, M. M. *Fuel Cell Engines*. (Wiley, 2008). doi:10.1002/9780470209769.
5. Rajaeifar, M. A., Ghadimi, P., Raugei, M., Wu, Y. & Heidrich, O. Challenges and recent developments in supply and value chains of electric vehicle batteries: A sustainability perspective. *Resources, Conservation and Recycling* **180**, 106144 (2022).
6. Cindrella, L. *et al.* Gas diffusion layer for proton exchange membrane fuel cells—A review. *Journal of Power Sources* **194**, 146–160 (2009).
7. Li, J., Fleetwood, J., Hawley, W. B. & Kays, W. From Materials to Cell: State-of-the-Art and Prospective Technologies for Lithium-Ion Battery Electrode Processing. *Chem. Rev.* **122**, 903–956 (2022).
8. Wanner, J., Weeber, M., Birke, K. P. & Sauer, A. Production planning and process optimization of a cell finishing process in battery cell manufacturing. *Procedia CIRP* **112**, 507–512 (2022).
9. Sharma, V. *et al.* Formulation graphs for mapping structure-composition of battery electrolytes to device performance. *Journal of Chemical Information and Modeling* **63**, 6998–7010 (2023).
10. Gonçalves, R., Lanceros-Méndez, S. & Costa, C. M. Electrode fabrication process and its influence in lithium-ion battery performance: State of the art and future trends. *Electrochemistry Communications* **135**, 107210 (2022).
11. Sarker, M. *et al.* Experimental and computational study of the microporous layer and hydrophobic treatment in the gas diffusion layer of a proton exchange membrane fuel cell. *Journal of Power Sources* **509**, 230350 (2021).
12. Schweiss, R., Meiser, C., Damjanovic, T., Galbiati, I. & Haak, N. *SIGRACET® Gas Diffusion Layers for PEM Fuel Cells, Electrolyzers and Batteries (White Paper)*. (2016).

13. Dominguez, D. Z. *et al.* Influence of the mixing speed in the rheology of NMC622-based Li-ion battery electrode slurries. *Journal of Power Sources Advances* **26**, 100141 (2024).
14. Paredes-Goyes, B. *et al.* Mesoscopic Model of Extrusion during Solvent-Free Lithium-ion Battery Electrode Manufacturing. *Batteries & Supercaps* **7**, e202300441 (2024).
15. Franco, A. A. Multiscale modelling and numerical simulation of rechargeable lithium ion batteries: concepts, methods and challenges. *Rsc Advances* **3**, 13027–13058 (2013).
16. Shodiev, A. *et al.* Designing electrode architectures to facilitate electrolyte infiltration for lithium-ion batteries. *Energy Storage Materials* **49**, 268–277 (2022).
17. Yoshimune, W., Kato, S., Inagaki, M. & Yamaguchi, S. A simple method to measure through-plane effective gas diffusivity of a gas diffusion layer for polymer electrolyte fuel cells. *International Journal of Heat and Mass Transfer* **191**, 122887 (2022).
18. Hwang, G. S. & Weber, A. Z. Effective-Diffusivity Measurement of Partially-Saturated Fuel-Cell Gas-Diffusion Layers. *J. Electrochem. Soc.* **159**, F683 (2012).
19. Mangal, P. *et al.* Experimental study of mass transport in PEMFCs: Through plane permeability and molecular diffusivity in GDLs. *Electrochimica Acta* **167**, 160–171 (2015).
20. Xia, L., Ni, M., He, Q., Xu, Q. & Cheng, C. Optimization of gas diffusion layer in high temperature PEMFC with the focuses on thickness and porosity. *Applied Energy* **300**, 117357 (2021).
21. Chen, Y., Jiang, C. & Cho, C. Characterization of Effective In-Plane Electrical Resistivity of a Gas Diffusion Layer in Polymer Electrolyte Membrane Fuel Cells through Freeze–Thaw Thermal Cycles. *Energies* **13**, 145 (2019).
22. Nitta, I., Himanen, O. & Mikkola, M. Thermal Conductivity and Contact Resistance of Compressed Gas Diffusion Layer of PEM Fuel Cell. *Fuel Cells* **8**, 111–119 (2008).
23. Román-Ramírez, L. A. & Marco, J. Design of experiments applied to lithium-ion batteries: A literature review. *Applied Energy* **320**, 119305 (2022).

24. Duquesnoy, M., Liu, C., Kumar, V., Ayerbe, E. & Franco, A. A. Toward high-performance energy and power battery cells with machine learning-based optimization of electrode manufacturing. *Journal of Power Sources* **590**, 233674 (2024).
25. Duquesnoy, M. *et al.* Machine learning-assisted multi-objective optimization of battery manufacturing from synthetic data generated by physics-based simulations. *Energy Storage Materials* **56**, 50–61 (2023).
26. Ayerbe, E., Berecibar, M., Clark, S., Franco, A. A. & Ruhland, J. Digitalization of battery manufacturing: current status, challenges, and opportunities. *Advanced Energy Materials* **12**, 2102696 (2022).
27. Sarkezi-Selsky, P., Rastedt, M., Latz, A. & Jahnke, T. Lattice-Boltzmann simulation of two-phase flows in the GDL and MPL of Polymer Electrolyte Fuel Cells. (2019).
28. Wu, W. & Jiang, F. Microstructure reconstruction and characterization of PEMFC electrodes. *International Journal of Hydrogen Energy* **39**, 15894–15906 (2014).
29. Hao, J. *et al.* Structural gradient optimization of diffusion layer based on finite data mapping method for PEMFC performance improvement. *International Journal of Heat and Mass Transfer* **220**, 124948 (2024).
30. www.erc-artistic.eu (ARTISTIC Project Webpage, accessed 2024-09-06).
31. Duquesnoy, M. *et al.* Machine learning-based assessment of the impact of the manufacturing process on battery electrode heterogeneity. *Energy and AI* **5**, 100090 (2021).
32. Duquesnoy, M., Lombardo, T., Chouchane, M., Primo, E. N. & Franco, A. A. Data-driven assessment of electrode calendering process by combining experimental results, in silico mesostructures generation and machine learning. *Journal of Power Sources* **480**, 229103 (2020).
33. Galvez-Aranda, D. E., Dinh, T. L., Vijay, U., Zanotto, F. M. & Franco, A. A. Time-Dependent Deep Learning Manufacturing Process Model for Battery Electrode Microstructure Prediction. *Advanced Energy Materials* **14**, 2400376 (2024).

34. Omongos, R. L., Galvez-Aranda, D. E., Zanotto, F. M., Vernes, A. & Franco, A. A. Machine learning-driven optimization of gas diffusion layer microstructure for PEM fuel cells. *Journal of Power Sources* **625**, 235583 (2025).

35. Niri, M. F. *et al.* Machine learning for optimised and clean Li-ion battery manufacturing: Revealing the dependency between electrode and cell characteristics. *Journal of cleaner production* **324**, 129272 (2021).

36. Nozarijouybari, Z. & Fathy, H. K. Machine learning for battery systems applications: Progress, challenges, and opportunities. *Journal of Power Sources* **601**, 234272 (2024).

37. F. Troncoso, J. *et al.* The ARTISTIC Battery Manufacturing Digitalization Initiative: From Fundamental Research to Industrialization. *Batteries & Supercaps* **n/a**, e202400385 (2024).

38. Cunha, R. P., Lombardo, T., Primo, E. N. & Franco, A. A. Artificial Intelligence Investigation of NMC Cathode Manufacturing Parameters Interdependencies. *Batteries & Supercaps* **3**, 60–67 (2020).

39. Primo, E. N., Touzin, M. & Franco, A. A. Calendering of Li (Ni0. 33Mn0. 33Co0. 33) O2-based cathodes: analyzing the link between process parameters and electrode properties by advanced statistics. *Batteries & Supercaps* **4**, 834–844 (2021).

40. Faraji Niri, M., Reynolds, C., Román Ramírez, L. A. A., Kendrick, E. & Marco, J. Systematic analysis of the impact of slurry coating on manufacture of Li-ion battery electrodes via explainable machine learning. *Energy Storage Materials* **51**, 223–238 (2022).

41. Faraji-Niri, M. *et al.* Accelerated state of health estimation of second life lithium-ion batteries via electrochemical impedance spectroscopy tests and machine learning techniques. *Journal of Energy Storage* **58**, 106295 (2023).

42. Petrich, L. *et al.* Crack detection in lithium-ion cells using machine learning. *Computational Materials Science* **136**, 297–305 (2017).

43. Furat, O. *et al.* Mapping the architecture of single lithium ion electrode particles in 3D, using electron backscatter diffraction and machine learning segmentation. *Journal of Power Sources* **483**, 229148 (2021).

44. Hou, L. F., Chen, H., Guo, H. & Ye, F. Multi-objective optimization of gas diffusion layer structure parameters for proton exchange membrane fuel cell. *International Journal of Green Energy* **21**, 787–797 (2024).

45. Shum, A. D., Liu, C. P., Lim, W. H., Parkinson, D. Y. & Zenyuk, I. V. Using Machine Learning Algorithms for Water Segmentation in Gas Diffusion Layers of Polymer Electrolyte Fuel Cells. *Transp Porous Med* **144**, 715–737 (2022).

46. Cawte, T. & Bazylak, A. A 3D convolutional neural network accurately predicts the permeability of gas diffusion layer materials directly from image data. *Current Opinion in Electrochemistry* **35**, 101101 (2022).

47. Froning, D., Wirtz, J., Hoppe, E. & Lehnert, W. Flow Characteristics of Fibrous Gas Diffusion Layers Using Machine Learning Methods. *Applied Sciences* **12**, 12193 (2022).

48. Saco, A., Sundari, P. S., J, K. & Paul, A. An Optimized Data Analysis on a Real-Time Application of PEM Fuel Cell Design by Using Machine Learning Algorithms. *Algorithms* **15**, 346 (2022).

49. Wang, J. *et al.* Integration of multi-physics and machine learning-based surrogate modelling approaches for multi-objective optimization of deformed GDL of PEM fuel cells. *Energy and AI* **14**, 100261 (2023).

50. Iman, M., Arabnia, H. R. & Rasheed, K. A review of deep transfer learning and recent advancements. *Technologies* **11**, 40 (2023).

51. Li, X. *et al.* Transfer learning in computer vision tasks: Remember where you come from. *Image and Vision Computing* **93**, 103853 (2020).

52. Wang, T. & Gan, V. J. L. Automated joint 3D reconstruction and visual inspection for buildings using computer vision and transfer learning. *Automation in Construction* **149**, 104810 (2023).

53. Laparra, E., Mascio, A., Velupillai, S. & Miller, T. A review of recent work in transfer learning and domain adaptation for natural language processing of electronic health records. *Yearbook of medical informatics* **30**, 239–244 (2021).

54. Qiu, M. *et al.* Easytransfer: a simple and scalable deep transfer learning platform for NLP applications. in 4075–4084 (2021).

55. Sahoo, S. *et al.* Transfer learning based generalized framework for state of health estimation of Li-ion cells. *Scientific Reports* **12**, 13173 (2022).

56. Liu, K. *et al.* Transfer learning for battery smarter state estimation and ageing prognostics: Recent progress, challenges, and prospects. *Advances in Applied Energy* **9**, 100117 (2023).

57. Briceno-Mena, L. A., Arges, C. G. & Romagnoli, J. A. Machine learning-based surrogate models and transfer learning for derivative free optimization of HT-PEM fuel cells. *Computers & Chemical Engineering* **171**, 108159 (2023).

58. Gong, Z. *et al.* Cross-domain diagnosis for polymer electrolyte membrane fuel cell based on digital twins and transfer learning network☆. *Energy and AI* **17**, 100412 (2024).

59. Ma, J. *et al.* Degradation prognosis for proton exchange membrane fuel cell based on hybrid transfer learning and intercell differences. *ISA Transactions* **113**, 149–165 (2021).

60. Zhuang, F. *et al.* A comprehensive survey on transfer learning. *Proceedings of the IEEE* **109**, 43–76 (2020).

61. Primo, E. N., Chouchane, M., Touzin, M., Vazquez, P. & Franco, A. A. Understanding the calendering processability of Li (Ni0. 33Mn0. 33Co0. 33) O2-based cathodes. *Journal of Power Sources* **488**, 229361 (2021).

62. Zapata Dominguez, D. *et al.* Influence of the mixing speed in the rheology of NMC622-based Li-ion battery electrode slurries. *Journal of Power Sources Advances* **26**, 100141 (2024).
63. Zapata Dominguez, D., Mondal, B., Gaberscek, M., Morcrette, M. & Franco, A. A. Impact of the manufacturing process on graphite blend electrodes with silicon nanoparticles for lithium-ion batteries. *Journal of Power Sources* **580**, 233367 (2023).
64. Pezoa, R., Salinas, L. & Torres, C. Explainability of High Energy Physics events classification using SHAP. *Journal of Physics: Conference Series* **2438**, 012082 (2023).
65. Dominguez, D. Z., Mondal, B., Gaberscek, M., Morcrette, M. & Franco, A. A. Impact of the manufacturing process on graphite blend electrodes with silicon nanoparticles for lithium-ion batteries. *Journal of Power Sources* **580**, 233367 (2023).
66. GeoDict - Modular software solution for digital material design. https://www.math2market.com/geodict-software/geodict-base-modules.html.
67. Rumelhart, D. E., Hinton, G. E. & Williams, R. J. Learning representations by back-propagating errors. *nature* **323**, 533–536 (1986).
68. Pang, B., Nijkamp, E. & Wu, Y. N. Deep learning with tensorflow: A review. *Journal of Educational and Behavioral Statistics* **45**, 227–248 (2020).
69. Saabith, S., Vinothraj, T. & Fareez, M. A review on Python libraries and Ides for Data Science. *Int. J. Res. Eng. Sci* **9**, 36–53 (2021).